




Water Content and Bedding Angle Effects on the Mechanical Properties and Micro-/Macro-Failure Mechanism of Phyllite

Long-Hao Ma^{1,2} · Jie Chen^{1,2} · Yun-Feng Zhao³ · Chuang Zhang^{1,2} · Rong Liu^{1,2} · Song Ren^{1,2} 

Received: 17 July 2021 / Accepted: 16 February 2022 / Published online: 28 March 2022
© King Fahd University of Petroleum & Minerals 2022

Abstract

The study of anisotropy and water degradation in phyllite is a prerequisite for excavation and support of phyllite tunnels. Previous studies have mostly analyzed the mechanical characteristics of phyllite under the action of water/laminae alone, but less research has been carried out on the macroscopic properties and microfracture evolution of phyllite under the action of coupled water-laminae. Therefore, the microstructure, mechanical behavior and fracture mode of phyllite were analyzed by polarized light and uniaxial experiments, and then SEM, acoustic emission (AE) and numerical tests of phyllite were carried out. The results indicate that (1) the elastic modulus of phyllite presents an asymmetric U-shape with bedding angle, with the maximum value of 0° and 90° and the minimum value of 60°. The peak strength shows two differentiation trends: U-shaped and nonlinear decreasing with bedding angle. (2) The peak strength and elastic modulus of phyllite are negatively correlated with water content. (3) The fracture mode of phyllite changes from compression shear failure to tensile failure with bedding angle. (4) The laminated structure and fish scale texture of phyllite tend to be discrete due to water erosion, which promotes the expansion of microcracks and weakens the mechanical parameters of the rock. (5) The change law of AE cumulative energy with bedding and water content is consistent with the change in macromechanical characteristics, which reveals the internal relationship between the progressive evolution of microcracks in rocks and macrofractures. The research results can provide an important reference for the construction scheme design, long-term stability, operation and maintenance of similar projects.

Keywords Phyllite · Water content · Bedding angle · Micro-/Macro-failure mechanism · PFC · AE

1 Introduction

Tunnels, oil and gas extraction, gas storage and other underground geotechnical engineering construction processes generally face two extremely difficult problems: one is the extreme geological conditions, such as partial pressure, large depth of burial, anisotropy, caves, etc., and the other is

the complex environmental conditions, such as high ground temperature, extreme cold, water-rich, gas, etc. In extreme geological drill and blast construction, it is easy to collapse, over or under excavate, separate layers and other unsafe events; in the complex environment for construction, water inrush and mud outburst, rock burst, frost heave deformation and other unstable phenomena easily occur. Among the above conditions, anisotropy (laminations) [1–7] and water are the most widely distributed, and the coupling of the two has a significant impact on the stability and safety of the rock mass [8–13]. Therefore, to ensure the safe construction, operation and maintenance of projects under similar geological and environmental conditions, it is necessary to investigate the mechanical characteristics, morphological characteristics and macro-/micro-rupture mechanisms of rocks under the coupling effect of anisotropy and water [14–16].

Currently, the influence of anisotropy on rock mainly focuses on mechanical properties and macrofracture characteristics. Some scholars have studied the influence of the

✉ Rong Liu
cqu_liurong@163.com

✉ Song Ren
rs_rwx@163.com

¹ School of Resources and Safety Engineering, Chongqing University, Chongqing 400030, China

² State Key Laboratory for the Coal Mine Disaster Dynamics and Controls, Chongqing University, Chongqing 400044, China

³ School of Urban Construction, Yangtze University, Jingzhou 434023, Hubei, China



bedding angle on the rock strength, elastic modulus, and failure mode in detail [17–21]. Subsequently, some studies [22–24] further analyzed the response characteristics of cumulative strain energy to the change in bedding angle. Ding et al. [25] studied the influence of foliation angles and loading angles on the mechanical characteristics and failure behavior of slate through a series of Brazilian disk tests and further discussed the variation trend of the anisotropy ratio and the coefficient of foliation effects under different foliation angles. Thus, they intuitively showed the significant degree of rock anisotropy changing with the foliation angle, but the disadvantage is that scanning only the fractured sample with an electron microscope could not invert the evolution process of rock microfractures.

Regarding the effect of water content on the mechanical properties of rocks, some scholars have studied the regularity of rock slope angle, strength, and modulus from water content [26–33]. Yu et al. [34] further studied the influence of water content and immersion time on the mechanical properties of red sandstone and found that the peak strength and elastic modulus have a negative exponential relationship with water content. Meanwhile, based on the creep tests of red sandstone under different water content, the accelerated crack growth mechanism of the water content was clarified. In addition, some studies revealed the influence of water-weakening effects on the mechanical parameters, fracture evolution process and failure mechanism of rock masses from the perspective of energy release and energy distribution [35, 36].

In summary, previous studies have lacked analyses that simultaneously consider the effects of water and laminae on the mechanical properties, micromorphology, microfracture evolution and macrofracture patterns of rocks, which has prevented us from better elucidating the superposition of both water and laminae on the weakening mechanisms, degree of deterioration and damage evolution of rocks. Furthermore, few of the existing studies have simultaneously used microfabrication techniques such as light microscopy, electron microscopic scanning, acoustic emission and discrete elements to further reveal the link between microfracture development and macroscopic fracture in phyllite in particular, and the existing studies have produced light microscopic thin sections and electron microscopic specimens with inadequate flatness, gold plating degree and staining, resulting in light microscopic images and electron microscopic photographs that do not well reflect the layered schistosity, silky luster and fish scale structure of the phyllite. Therefore, the deep-buried carbonaceous phyllite through which the Zhegu Mountain tunnel passes, an important joint project of the Wenchuan–Maerkang Expressway, was taken as the research object in this study. Based on the design of the mechanical test scheme of the bedding surrounding rock in the existing literature and taking into account the internal structure and clay

mineral composition of the rocks that are susceptible to deterioration by water, uniaxial compression experiments were designed and carried out on rocks at different laminar angles and water conditions. The macroscopic mechanical properties, fracture mechanisms and fracture modes of the phyllite were obtained under different laminar angles and water conditions. Through the above experimental studies, we have a clear understanding of the macroscopic failure mechanism and failure characteristics of phyllite under the coupled action of water and laminae, but like most of the existing studies, we only analyze the macroscopic mechanical level, and the specific connection between the evolution of microscopic cracks and macroscopic fracture is not yet clear. In view of this, this paper investigates the extension process, type, distribution form and final damage pattern of microfractures within phyllite under different water-bearing states and different lamination angles with the help of the microfracture calculation program PFC, thus initially revealing the relationship between microcrack development and macrofracture formation. Subsequently, the impact of the microstructure of the matrix and propagation of microcracks on the macromechanical behavior of phyllite was further investigated by SEM scanning and AE to demonstrate the intuitive relationship between the microscopic fracture mechanism and macrofracture.

2 Experimental Methods

2.1 Sample Preparation

The phyllite used in the test was taken from the Zhegu Mountain tunnel, a critical project of the Wenchuan–Maerkang Expressway in Sichuan Province. The tunnel is 8784 m in length, 13.4 m in width and 10.5 m in height and has a maximum depth of 1300 m. The phyllite of the tunnel is dark gray in color and has a variable argillaceous-weak plate structure.

Due to the unique laminar sedimentary structure of phyllite, the specimen formation rate is very low, so phyllite specimens with bedding directions and axial directions of 0°, 30°, 60°, and 90° are drilled (Fig. 1a). The main mineral composition of carbonaceous phyllite specimens was determined by X-ray diffraction and comprised chlorite (48%), illite (38%), quartz (10%) and plagioclase (4%). The specimens taken from the phyllite were processed into standard cylindrical specimens with a diameter of 50 mm and length of 100 mm, with an error of ± 0.5 mm. The prepared phyllite specimens are shown in Fig. 1b. To observe the microstructure of phyllite, the prepared phyllite was cut into four groups of thin sections along the axial and radial directions (Fig. 1c). Then, the prepared thin sections were placed under a polarized light microscope (Fig. 1d), and the microscopic characteristics of the local area of the sample were observed

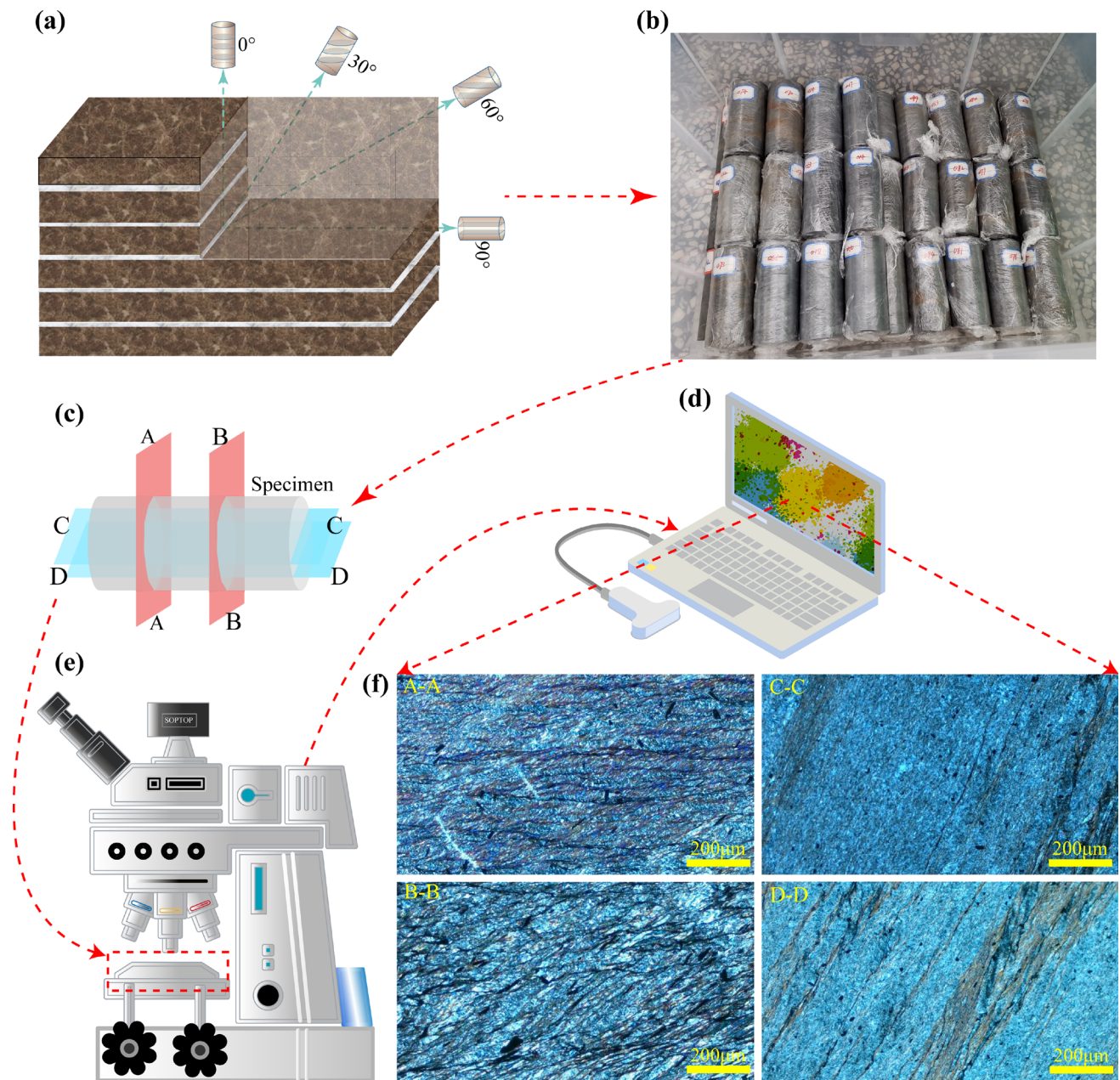


Fig. 1 Specimen preparation and polarized micrograph of phyllite. **a** Schematic diagram of the drilling in different directions; **b** Prepared samples; **c** Rock slice; **d** Polarizing microscope; **e** Laptop; **f** Rock microstructure

by computer in real time (Fig. 1e). The microstructure of the phyllite samples is shown in Fig. 1f. It can be seen that the microstructure of the phyllite presents fish-scale or fold-like textures, with well-developed bedding and weak satin luster.

To fully investigate the water softening characteristics of phyllite, three water-bearing states, including drying, soaking and saturated, were designed in the tests. Two specimens were prepared for each state. The specimen in a drying state is placed in an oven at 105 °C for 24 h until the mass of the specimen is no longer changed. According to the provisions on dried samples in ISRM, [37] the moisture content of the

sample is considered to be 0%. The specimen in a soaking state is immersed in water for 24 h, and the corresponding moisture content of the sample is measured and calculated to be approximately 1.5%. The specimen in a saturated state was heated in a drying oven at 105 °C for 24 h and then vertically placed in a vacuum saturation pressurization device at pH = 7 for water absorption under full pressure for 24 h. Subsequently, the mass of the specimens under full water and drying was measured using an electronic balance with an accuracy of 0.01 g, and the saturated water content was calculated to be 2.7% according to equation $\omega_s = \frac{m_s - m_d}{m_d} \times 100\%$.

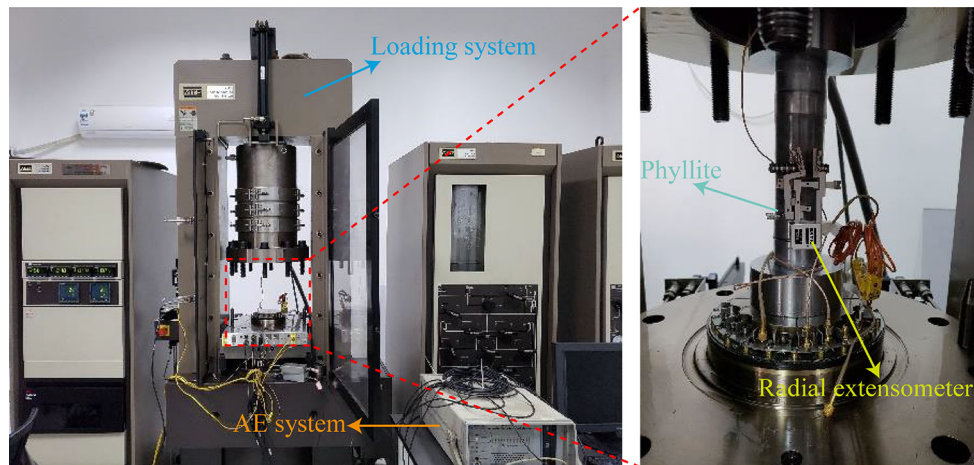


Fig. 2 MTS815 rock mechanical system and AE system

Table 1 Parameters of the AE system

Data transmission speed (MB/s)	Trigger processing capability (MFLOPS)	Lowest noise threshold (dB)	Frequency range (kHz)	High processing speed (hits/s)	PDT (μs)	HDT (μs)	HLT (μs)	Threshold value (dB)
132	150	18	10 ~ 2100	20,000	35	150	300	40

Table 2 Parameters of the sensor

Size (mm \times mm)	Suitable operating temperature ($^{\circ}\text{C}$)	Hit limit	Peak sensitivity (V/Pa)	Operating frequency range (kHz)	Directional awareness (dB)
10 \times 12	- 65 ~ 177	10,000	- 650	175 ~ 1000	± 1.5

In addition, after the specimens are processed, their surfaces are wrapped with multilayer plastic wrap and waterproofing membranes to ensure that there is no loss of water.

2.2 Testing Apparatus

The uniaxial compression experiment was carried out with the MTS 815 rock mechanics test system (Fig. 2). Its axial maximum load is 2800 kN, and its maximum confining pressure is 80 MPa. The AE test was conducted using the DISP series 2 channel/card PCI-2 fully digital AE monitoring system. The system parameters are shown in Table 1. To ensure the test effect, two channels were used in the test. Each channel corresponds to a separate preamplifier and transducer, where the amplifier adopts the American acoustic company's differential 20/40/60 dB gain preamplifier, and the acoustic signal pregain is 40 dB. The sensor is a nano30 micropiezoelectric transducer with a working frequency range of 150 kHz ~ 400 kHz and a peak sensitivity of 62 dB. In addition, the nano30 sensor introduces three parameters, PDT, HDT and HLT, which represent the signal

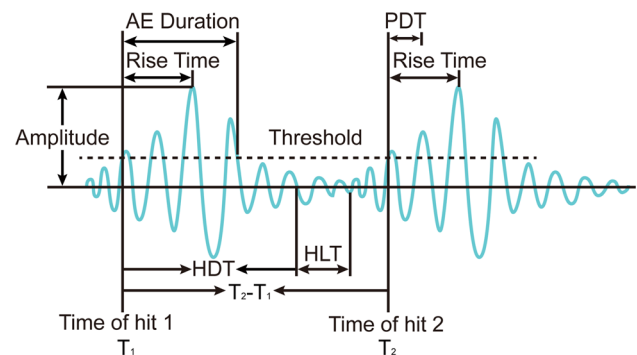


Fig. 3 AE hit feature diagram

peak definition time, hit definition time and hit locking time, respectively (Fig. 3). Reasonable setting of PDT can ensure the correct identification of signal peak rise time and accurate measurement of peak amplitude, and if the rise time is greater than PDT, the captured amplitude will be less than the true value. Proper setting of HDT can ensure that each AE signal in the data structure corresponds to one and only

one hit event. Accurate setting of HLT can avoid spurious detection in the process of signal attenuation and improve the data acquisition speed. According to the suggestion of the American Acoustics Company, the PDT, HDT and HLT are taken to be 35 μs , 150 μs and 300 μs , respectively [38, 39]. Other parameters of the sensor are shown in Table 2. In addition, considering the effect of ambient noise on the acoustic emission test, this paper performed several sets of blank control experiments before the start of the compression test, which detected an AE signal threshold of 40 dB.

2.3 Experimental Program

To investigate the mechanical properties and failure mechanism of phyllite for different bedding angles and water content, tests with different bedding and water content were carried out using the MTS815 servo loading system and controlled through axial displacement at a constant loading rate of 0.05 mm/min. Before the compression test, the NANO-30 acoustic emission sensors were symmetrically arranged at the end of the specimen, and a thin layer of Vaseline was coated on the acoustic coupling sensors. Then, the two sensors were fixed with rubber bands. After the above steps were completed, the axial displacement, axial force, circumferential displacement and AE hit signals were synchronously collected.

3 Experimental Results

As shown in Table 3, under dry conditions, as the lamination angle θ changed from 0° to 90° , the UCS changed from 54.45 to 42.58 MPa, which is a reduction of 21.8%; the modulus of elasticity changed from 9.01 to 6.38 GPa, which is a reduction of 29.2%. At $\theta = 0^\circ$, when the water content changed from dry to saturated, the corresponding UCS changed from 54.45 to 36.95 MPa with a decrease of 32.1%, and the elastic modulus changed from 9.01 to 3.09 GPa, with a decrease of 65.7%. It can be concluded from the above analysis that the moisture content and bedding angle have a significant influence on the mechanical properties of phyllite specimens.

3.1 Effect of Bedding Angle on Macroscopic Mechanical Properties of Phyllite

The entire failure process of the phyllite specimens for different bedding angles can be roughly divided into four stages (see Fig. 4a, b): the initial pore compaction stage, linear elastic phase, plastic yielding phase, and brittle failure phase. Because the displacement loading method was used in the experiment, the initial compaction phase at each layering angle is more evident. With the increase in displacement, the

sample enters the linear elastic phase, in which the stress–strain curve exhibits a rapid growth trend and occupies most of the entire compression process. After the loading stress reaches the peak stress of the sample, the bearing capacity of the phyllite is promptly reduced, and the specimen is destroyed rapidly, which indicates that phyllite has typical brittle failure characteristics.

Figure 5 shows the corresponding relationship between the peak strength and elastic modulus with respect to the bedding angle. When the bedding angle θ is increased from 0° to 30° , the peak strength of phyllite under dry, watery and water-saturated conditions is reduced by 8.6%, 18.8%, and 35.0%, respectively. From $\theta = 30^\circ$ to 60° , the peak strength is reduced by 35.3%, 41.1%, 53.8%, respectively. From 60° to 90° , the strength is increased by 32.3%, 11.3%, and 3.8%, respectively. In addition, it is observed that when the water content is 0%, the compressive strength and elastic modulus of phyllite show a "U-shaped" trend with increasing bedding angle. As the water content gradually increases from 0 to 2.7%, the change trend of the compressive strength and elastic modulus of phyllite differentiates; among them, the elastic modulus still presents a typical "U-shaped" trend with increasing bedding angle, [40, 41] while the uniaxial compressive strength approximately shows a nonlinear decreasing trend.

3.2 Influence of Water Content on Macroscopic Mechanical Properties of Phyllite

According to the mineral composition analysis of phyllite, the proportion of clay in phyllite is very large. When it contacts water, it will soften, resulting in the weakening of friction between phyllite mineral particles and the reduction of resistance in the material itself. Macroscopically, it shows that the mechanical properties of phyllite are weakened.

Figure 6 shows the stress–strain curves of specimens for bedding angles of 0° and 90° . The following can be observed: (1) with increasing water content, the original voids and cracks inside the rock are continuously eroded. The increase in the volume of the initial pores and fissures leads to an increase in the strain in the initial compaction stage, and the compression characteristics of the rock are more apparent. (2) Under different water content, the phyllite has no obvious plastic yield behavior and mainly exhibits elastic deformation before reaching the peak strength. (3) After the peak, the brittleness of phyllite under dry and natural conditions is considerable. However, under saturated conditions, the ductile characteristics of phyllite are significantly enhanced.

It can be observed from Fig. 7 that the peak intensity and elastic modulus of phyllite decrease linearly with increasing water content, which also indicates that water content has a significant weakening effect on the mechanical properties of phyllite. Therefore, to minimize the impact of blasting

Table 3 Results of the uniaxial compression experiment

	Specimen	Moisture content (ω)	Angle (θ)	UCS (MPa)		Elastic modulus (GPa)	
				Tested	Average	Tested	Average
	D1-1	Dry	0°	54.07	54.45	8.55	9.01
	D1-2	Dry	0°	54.83		9.47	
	D2-1	Watery	0°	46.92	47.31	6.74	7.01
	D2-2	Watery	0°	47.70		7.28	
	D3-1	Saturate	0°	36.97	36.95	3.02	3.09
	D3-2	Saturate	0°	36.93		3.16	
	D4-1	Dry	30°	49.04	49.75	4.98	5.08
	D4-2	Dry	30°	50.46		5.18	
	D5-1	Watery	30°	38.26	38.39	3.04	3.24
	D5-2	Watery	30°	38.52		3.44	
	D6-1	Saturate	30°	23.98	24.01	2.27	2.34
	D6-2	Saturate	30°	24.04		2.41	
	D7-1	Dry	60°	32.86	32.19	6.14	6.06
	D7-2	Dry	60°	31.52		5.98	
	D8-1	Watery	60°	22.35	22.59	3.16	3.27
	D8-2	Watery	60°	22.83		3.38	
	D9-1	Saturate	60°	10.32	11.09	1.67	1.97
	D9-2	Saturate	60°	11.86		2.27	
	D10-1	Dry	90°	42.29	42.58	6.27	6.38
	D10-2	Dry	90°	42.87		6.49	
	D11-1	Watery	90°	25.61	25.14	2.81	2.60
	D11-2	Watery	90°	24.67		2.39	
	D12-1	Saturate	90°	11.65	11.52	2.16	2.07
	D12-2	Saturate	90°	11.39		1.98	

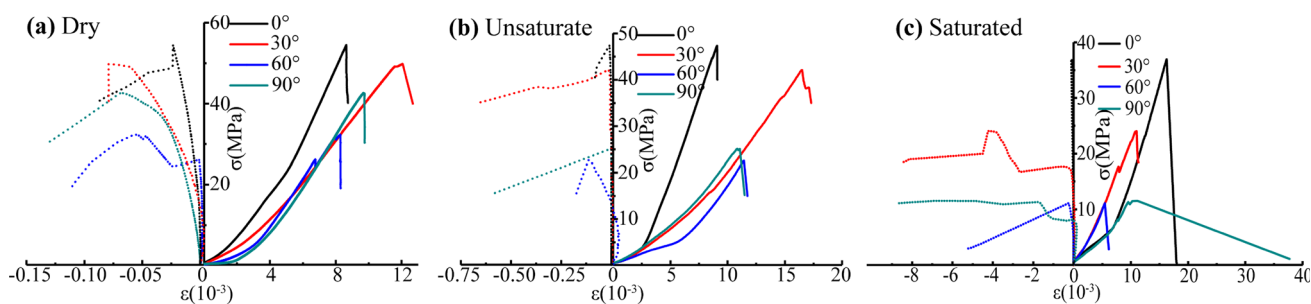


Fig. 4 Stress–strain curves of phyllite for different bedding angles

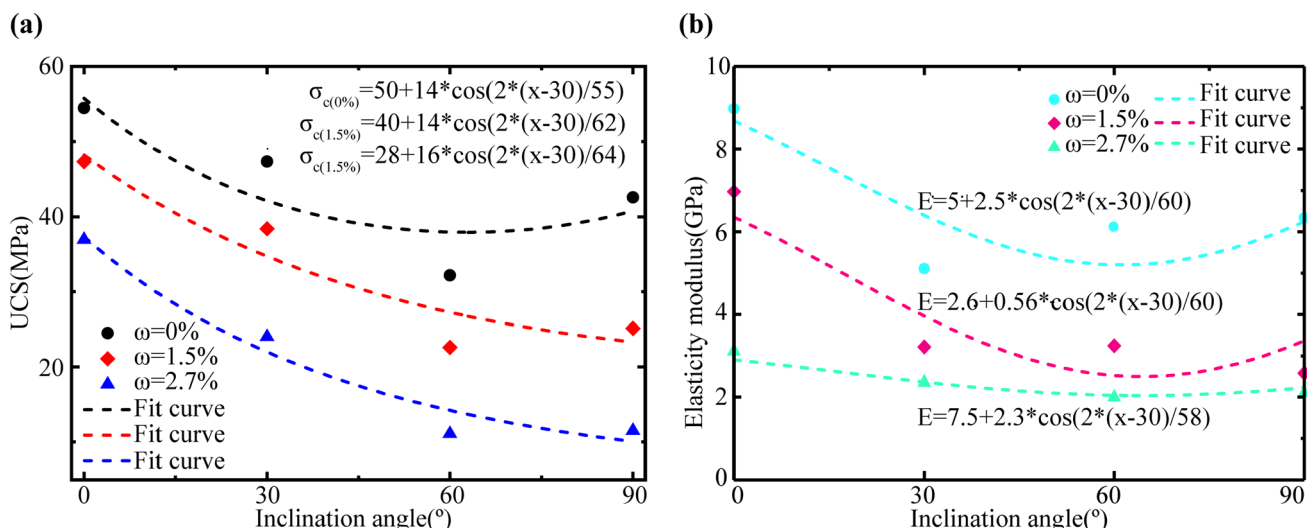


Fig. 5 Variation in the mechanical parameters of phyllite with bedding angle. a UCS; b Elastic modulus

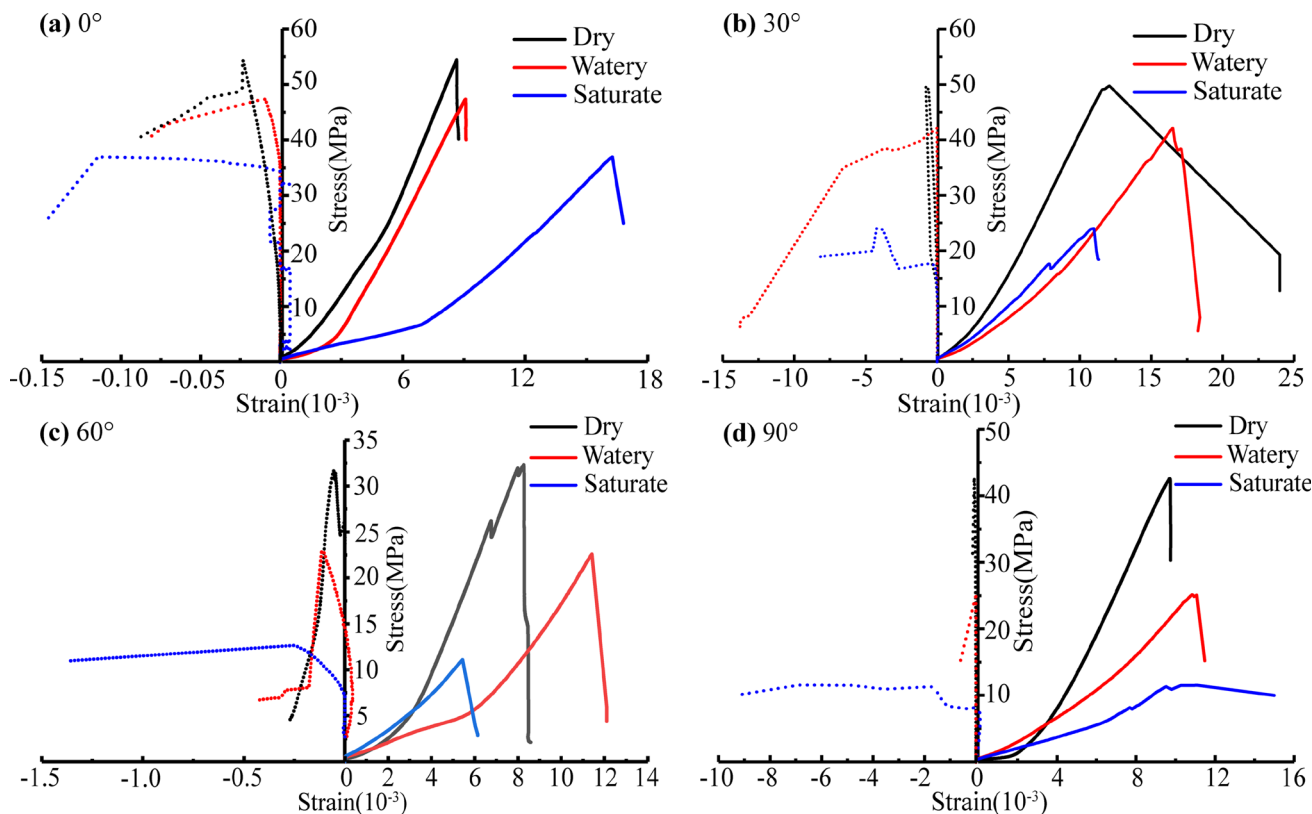


Fig. 6 Stress–strain curves of phyllite for different water content

on the surrounding rocks during the construction of the tunnel through phyllite stratum, it is necessary to control the blasting parameters of the section undergoing actual construction, such as single-cycle blasting charge, differential, hole spacing, wire charge density, etc. [42, 43] In addition, advanced prereinforcement technology can possibly be used

to strengthen the core soil of the tunnel palm face and effectively control the convergence deformation of the tunnel.

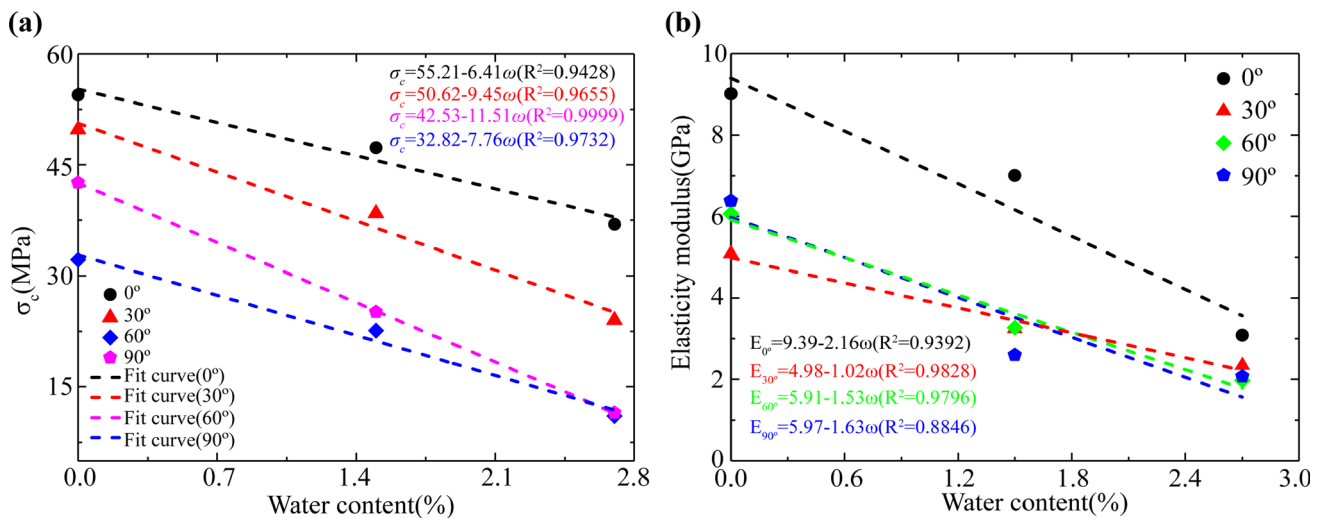


Fig. 7 Variation in the mechanical parameters of phyllite with water content. **a** UCS; **b** Elastic modulus

3.3 Fracture Pattern

3.3.1 Failure Modes of Phyllite for Different Bedding Angles

As shown in Fig. 8a, when the bedding angle is 0°, the final failure mode of the specimen is dependent on delamination shear failure of the matrix, and the crack surface penetrates the rock material and bedding surface. When the bedding angle is 30°–60°, the crack surface is connected with the lateral free surface of the specimen to form a penetrating fracture surface at the upper end of the sample. When the bedding angle is 90°, the failure form of the phyllite sample is mainly longitudinal splitting failure, and a macroscopic crack surface is formed with the initiation and propagation of tensile microcracks in the process of failure. This phenomenon is consistent with the observed results [17]. From the point of view of the failure mode, the weak cementation of the bedding surface plays a leading role in the failure mechanism and strength.

In addition, when the specimen changes from dry to water-bearing and saturated water (Fig. 8a, b, c), the fracture mode of the phyllite gradually changes from a single through-bedding shear slip fracture mode (0°–60°) or tension fracture mode to a mixed fracture mode of shear slip and tension fracture. The above phenomenon fully demonstrates that under dry conditions, the brittleness of phyllite with different bedding angles is very significant, and it is prone to single shear fracture and tension fracture. However, with the continuous increase in water content, the ductility of phyllite is strengthened, and the brittleness is weakened, which in turn leads to mainly shear failure, accompanied by a certain tensile failure.

3.3.2 Failure Patterns of Phyllite for Different Moisture Content

Figure 9 shows the typical failure modes of phyllite for different water contents. Under dry and soaking conditions, the failure mechanism of phyllite is mainly longitudinal tensile-cracking failure, accompanied by a “step”-like lateral injury. Under saturated states, the macroscopic fracture surface of phyllite is a single penetrating tensile failure surface. However, on the whole, whether dry, watery, or saturated, the main failure modes and failure mechanisms of phyllite are basically consistent, which indicates that the water content has little effect on the failure mode of phyllite. Furthermore, it can be observed from Fig. 9 that the number of longitudinal tensile cracks of the phyllite and the extended characteristics of the secondary cracks in the different water-containing states are considerably different. Therefore, the influence of water on the failure law of phyllite can be studied from the perspective of crack propagation.

Crack propagation in the three water conditions involves a main penetrating crack controlled by the lamination surface, and several nonpenetrating secondary cracks developed near the main crack. Among these, the cracks under dry conditions are densely distributed along the radial direction, and there are prominent main cracks on the free surface of the middle and left sides of the specimen. The main cracks bifurcate during the expansion process, and multiple secondary cracks are derived. The distribution of cracks under unsaturated and saturated water conditions is basically the same as that under dry conditions, although the number of cracks is much lower.

In summary, the bedding angle and moisture content have a great influence on the failure mode of phyllite. However, the lateral focus is different. The bedding angle is more inclined

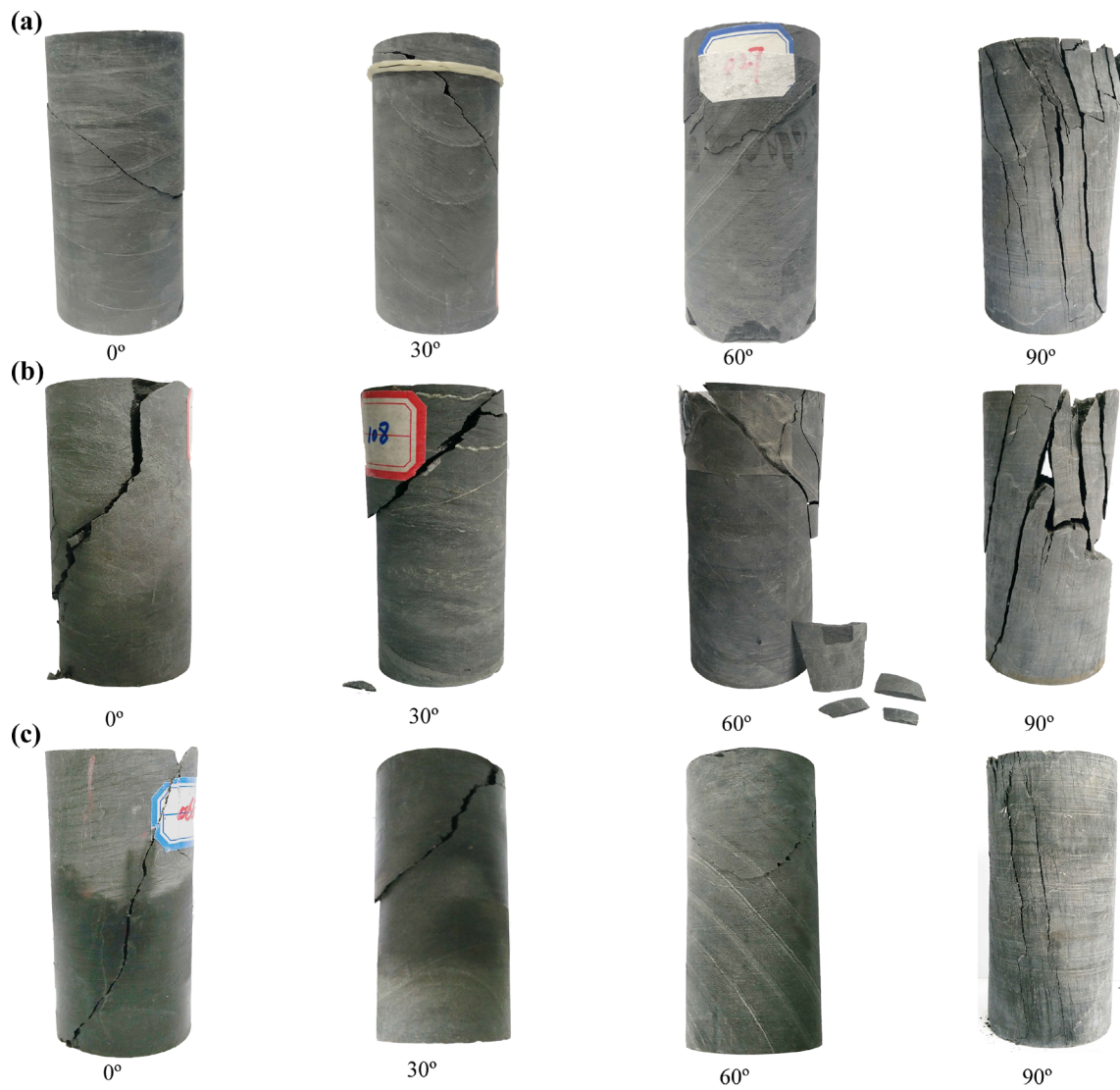


Fig. 8 Failure modes of different layers of phyllite. **a** Dry condition (0%); **b** Unsaturated condition (1.5%); **c** Saturated condition (2.7%)

Fig. 9 Uniaxial compression failure modes of phyllite for different water content (90°)



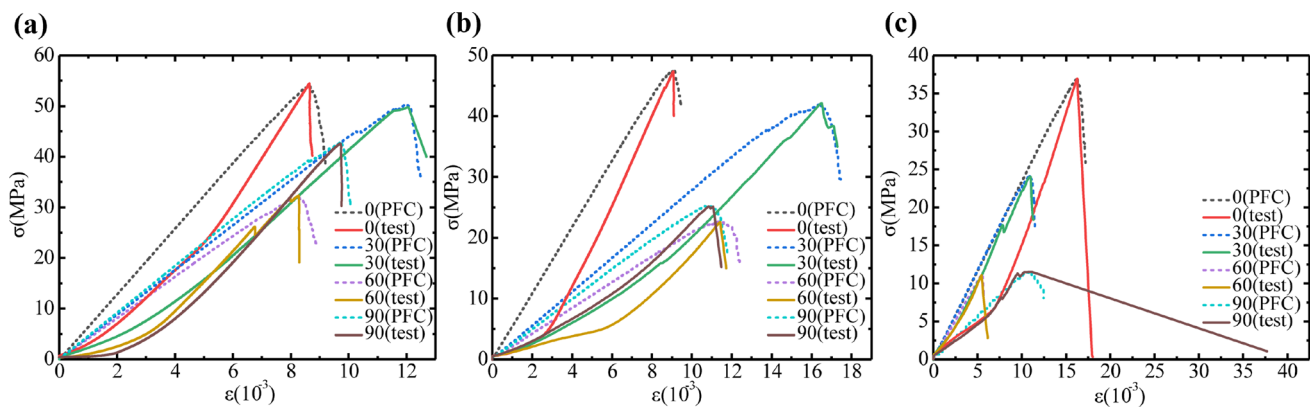


Fig. 10 Comparison of stress–strain curves under PFC and experimental conditions. **a** Dry; **b** Watery; **c** Saturated

to control the failure types of phyllite, such as shear failure and tensile failure, whereas the water content controls the secondary crack propagation and the number of cracks in phyllite. Therefore, when constructing a tunnel in a layered or water-bearing stratum, pre-reinforcement and advance support of the soft bedding plane should be carried out first, and the integrity of the bedding plane and bedrock should be strengthened to improve the anti-frictional force of the bedding plane.

3.4 Particle Discrete Element Modeling of Uniaxial Compression

In the previous sections, the macrofailure mode of phyllite under uniaxial compression was analyzed in detail. However, the relationship between the formation of macrofractures and the propagation mechanism of microcracks is not very clear. Considering this, further analysis is carried out on the failure mechanism of phyllite from the micro-level, and the discrete element method is adopted to simulate the failure mechanism of phyllite. The mechanism of propagation and development of microcracks in phyllite under uniaxial compression is analyzed.

Particle Flow (PFC) is a numerical calculation program based on the discrete element method, [44, 45] which characterizes the macroscopic mechanical properties of granular materials by defining the bonding behavior and bonding parameters between rigid particles [46, 47]. The actual rock in the formation is composed of solid mineral particles through a certain form of connection. Therefore, PFC can be used to simulate the micromechanical behavior of the particles in the rock. By establishing the bond relationship between the particles, the fracture behavior after contact failure between particles can be realized, thus reflecting the macroscopic crack propagation of rock materials.

With the help of embedded Fish language, uniaxial compression models of rocks with different bedding angles are

established. The size of the model is 50×100 . The particles in the model are randomly distributed, and the size distribution range is $0.4 \sim 0.6$ mm. The particle density is 1600 kg/m^3 , the particle porosity is 0.03 and the particle friction coefficient is 0.75. The minimum radius and maximum radius of the particles are 0.4 mm and 0.6 mm, respectively, and the corresponding particle size ratio is 1.5. The model includes a thick dense layer and a thin loose layer. Parallel bonding is used for the dense stratification model to simulate the tight matrix of rock, where the stiffness ratio of parallel bonding is 2.5 and the tensile strength is 56 MPa. The loose layer is simulated using a smooth joint model with a normal/tangential stiffness ratio of 1.2 and a tensile strength of 9 MPa for the joint.

To ensure the reliability and effectiveness of the numerical test, the trial-and-error method is used to continuously adjust the rock microscopic parameters until the stress–strain curve and failure mode of the numerical simulation are consistent with the results of the indoor test. The adjusted rock stress–strain curve and failure mode are shown in Figs. 10 and 11. The simulated stress–strain curve and failure mode are basically consistent with the actual experimental curve. The elastic modulus and peak strength are in good agreement with the actual experimental results, but the deficiency is that the compaction stage of the simulation curve is not obvious. This is mainly because the model itself needs to prepare the sample first, in which the process needs to conduct a balance treatment on the sample, that is, squeeze such macro-defects as open cracks and pores in the sample. After the completion of extrusion process, it is hard for the initial calculation model to contain open cracks, so there will be no obvious compaction stage. Secondly, it is a meso contact model rather than a macro-model, reflecting only the contact relationship between rigid particles. As a consequence, in the initial stage of the compressive process, the contact between particles has occurred, so that it cannot reflect the initial compaction characteristics. In addition, it can be observed from



Fig. 11 Failure mode of phyllite under PFC. **a** Dry; **b** Watery; **c** Saturated water

Fig. 11 that the main failure mode of phyllite is tensile fracture, accompanied by shear fracture. The microcracks under different water-bearing conditions and different bedding layers develop preferentially from the diagonal region of the specimen. With the increase in axial load, the microcracks in the diagonal region of the specimen continue to develop and expand until macroscopic fracture occurs. However, in the previous failure mode analysis, it is too subjective to conclude that phyllite is fractured by a single tensile or shear

only depending on the final failure mode of the specimen. Based on the above analysis, we can intuitively and accurately understand the development process, aggregation form and type of microcracks in the specimen instead of simply judging the failure mechanism of the specimen based on the fracture results after the test.

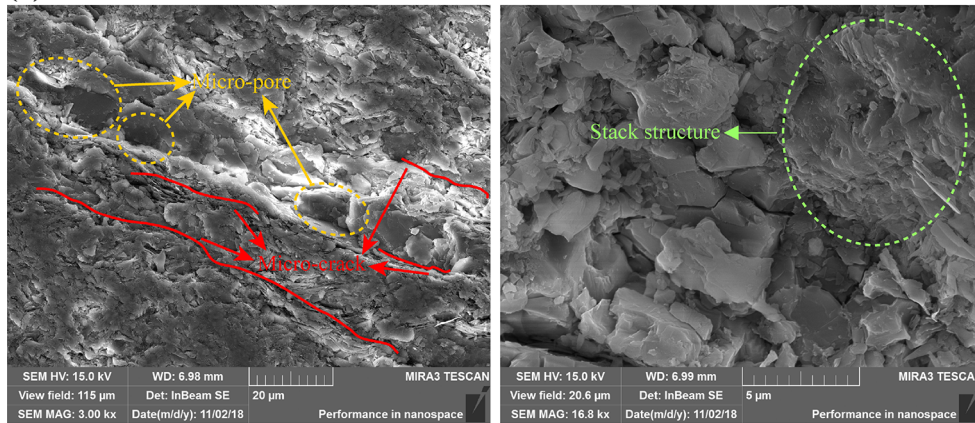
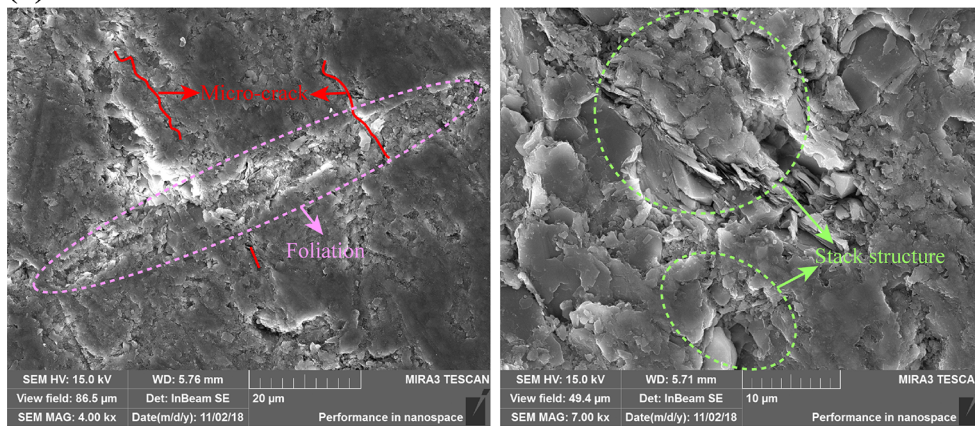
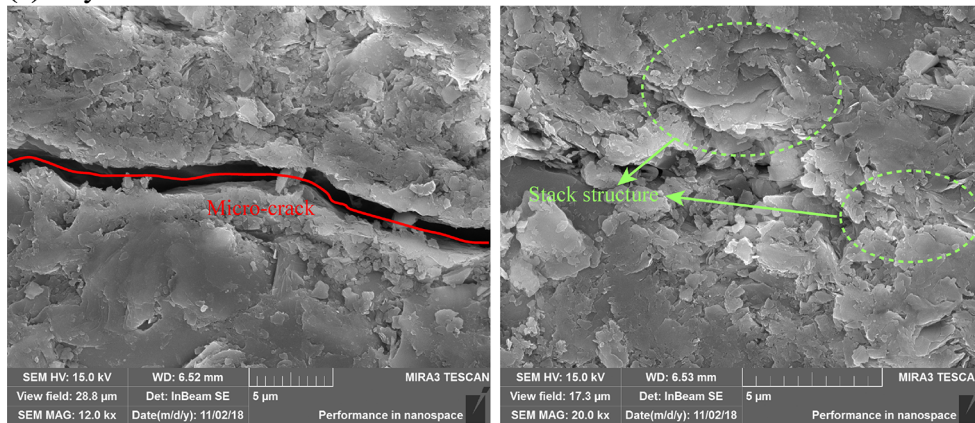
(a) Saturated**(b) Unsaturated****(c) Dry**

Fig. 12 Microstructure of phyllite. **a** Saturated; **b** Unsaturated; **c** Dry

4 Discussion

4.1 Analysis of Mechanical Characteristics Based on Electron Microscopy

The macroscopic mechanical characteristics of rocks are essentially the concrete forms of rock microstructure; in other words, the change in microstructure will eventually lead to

the change in macroscopic mechanical properties [48–52]. In this study, the microstructure, [53, 54] microfracture patterns and microfracture mechanism of phyllite were analyzed by scanning electron microscopy. The magnification was set to 3000 \times , 6000 \times , and 9000 \times . Figure 12 shows that the microstructure of phyllite is a layered or lamellae-stacked structure with clear micropores and microfissures, wherein the fissures are similarly arranged in parallel and the pores

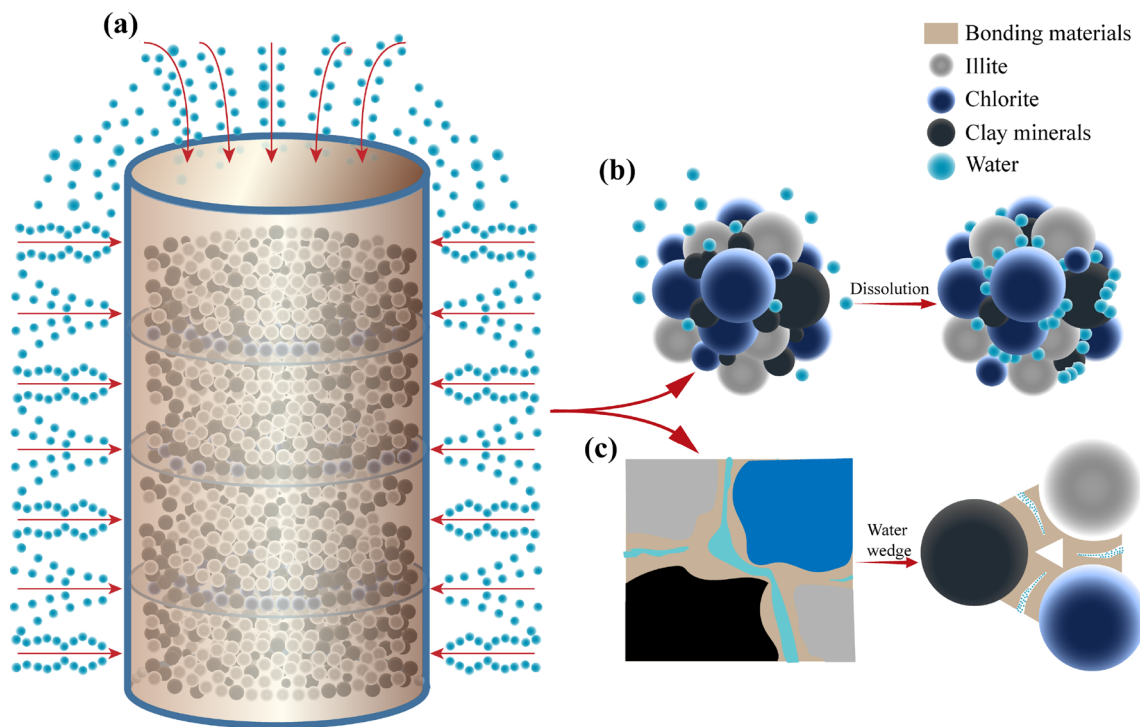


Fig. 13 Weakening mechanism of phyllite by water. **a** Water molecules invading the interior of rocks; **b** Hydrolysis; **c** Water wedge

are distributed along a straight line. The number of fissures is greater than the number of pores. To further analyze the difference in rock microstructure in each water state, the electron micrographs were analyzed in detail. Figure 12a shows three micropores and four microcracks. The shape of the micropores is almost square and not regular. The average micropore diameters are approximately 1.8 μm, and the maximum and minimum microcrack lengths are approximately 18 and 3 μm, respectively, with an approximate average value of 7.8 μm. Two microcracks are shown in Fig. 12b, while the surface delamination is very distinct and the extent of their boundaries in the matrix is relatively easy to determine. A clear single microcrack can be seen in Fig. 12c, which has good linearity and small local bending, and the crack width is approximately 0.4 μm. It can be seen from the distribution number of microcracks that the number of microcracks in phyllite increases gradually with increasing water content. At the same time, it should also be noted that when the water content is low, the phyllite matrix space is closely distributed with only a small amount of micropores. The above situation shows that due to the invasion of water, the water-soluble cementitious materials and clay minerals between rock particles begin to hydrolyze, resulting in the discretization of the initial dense matrix space (Fig. 13a–b). The discretization of matrix space induces the following two effects. On the one hand, with the increase in loose particles, more secondary micropores and secondary microcracks are generated in the rock, which provide seepage channels for the further

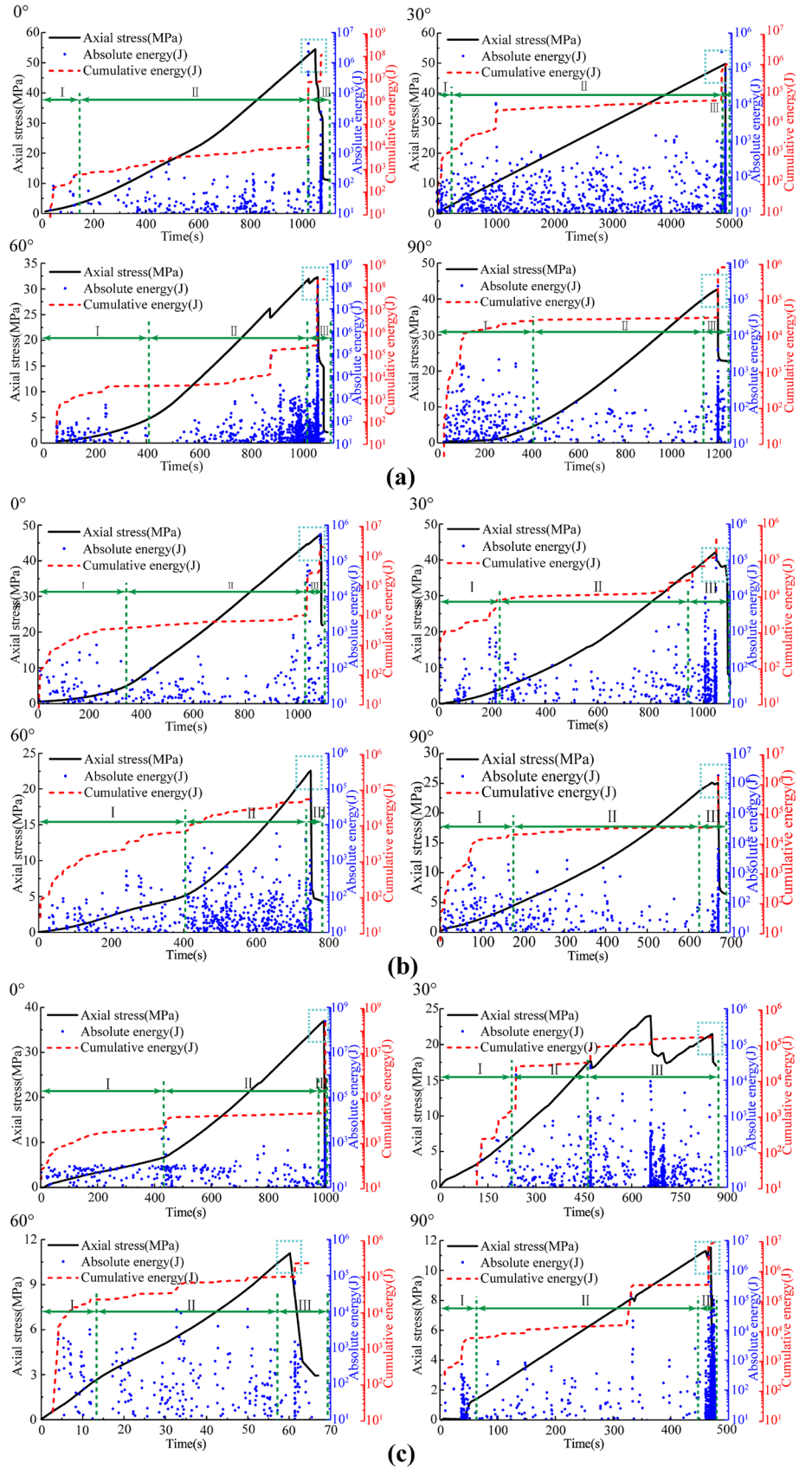
erosion of water molecules. On the other hand, with the continuous erosion of water molecules, the stress concentration effect at the tip of microcracks becomes increasingly obvious, which promotes the further expansion and extension of microcracks, which intensifies the microdamage in rock and the weakening effect of the mechanical parameters of phyllite [55, 56]. In addition, according to the Mohr Coulomb criterion $\tau = c + \sigma \tan \varphi$, $\varphi = 2\alpha - \frac{\pi}{4}$, the shear strength of rock is related to cohesion and internal friction angle, while the cohesion between particles of rock affected by water decreases, resulting in a decrease in rock shear strength.

4.2 Analysis of Mechanical Characteristics Based on Acoustic Emission (AE)

The change process of acoustic emission impact events directly reflects the generation, propagation and final fracture of microcracks in rock. Therefore, the damage evolution process of rock can be clarified by analyzing the acoustic emission characteristics of each mechanical stage of rock [54]. In addition, considering the accumulation, release and loss of rock elastic energy in the process of compression, this paper studies the internal relationship between microcrack accumulation, propagation processes and macrofractures from the perspective of acoustic emission cumulative energy [57].

Figure 14 shows the stress-time, AE absolute energy-time and AE cumulative energy-time curves for uniaxial

Fig. 14 AE characteristics of different layered phyllite under dry conditions. **a** Dry conditions; **b** Unsaturated conditions; **c** Saturated conditions



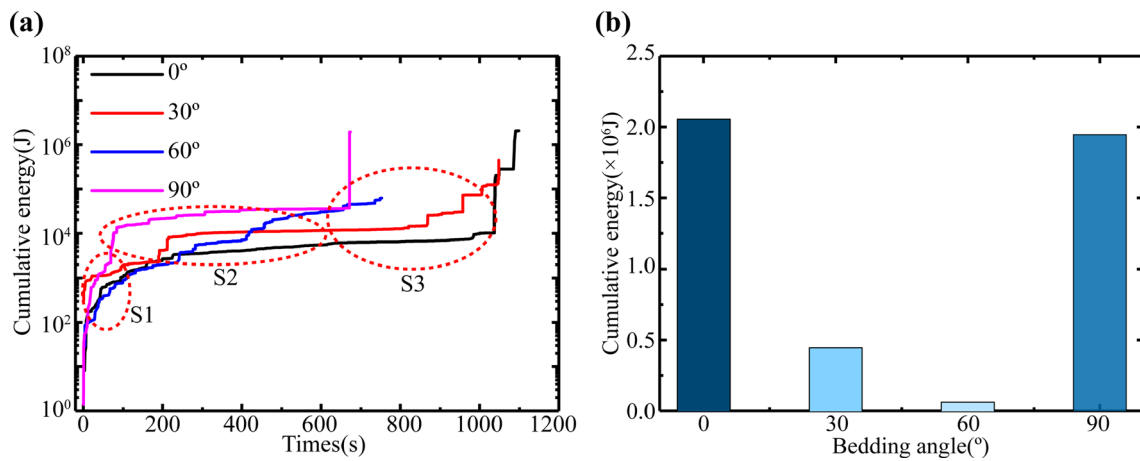


Fig. 15 Cumulative energy of phyllite at different bedding angles (watery state). **a** variation of cumulative energy; **b** relationship between cumulative energy and bedding angles

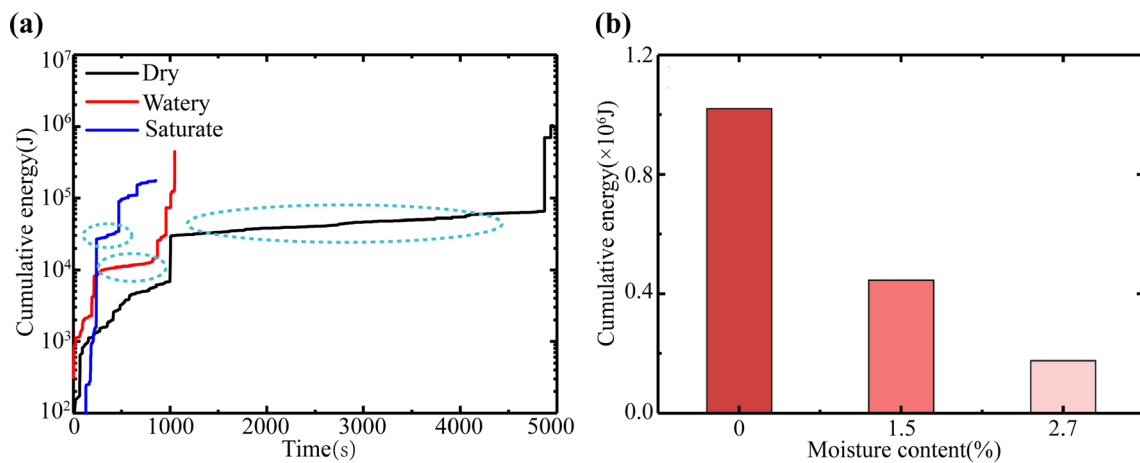


Fig. 16 Cumulative energy of phyllite at different moisture content. **a** variation of cumulative energy; **b** relationship between cumulative energy and moisture content

compression of different layered phyllite samples under different moisture conditions. The variation law of the entire AE energy corresponds to the fracture compaction phase (I), elastic deformation phase (II), and failure phase (III) in the complete stress–strain curve. In the compaction phase, the stress on the rock specimen is small, and no new cracks are generated in its internal structure. Therefore, the AE signal received in the closed phase is small, and the energy level is low ($10^1 \sim 10^3$), mainly for friction AE. With the increase in axial stress, the specimen enters the stage of elastic deformation. In this phase, the layered rock is prone to stress concentration at the bedding plane, and microcracks sprout along the bedding plane, releasing a certain amount of AE energy. After the elastic wave is released, the newly generated crack is pressed again, so the AE energy amplitude in the elastic phase is also relatively low (approximately 10^3). Because there is no obvious plastic yield point of phyllite, when the stress reaches a certain value, the specimen

directly enters the failure stage. In this phase, the rock sample immediately undergoes overall instability failure, and the AE energy amplitude reaches the maximum value of the entire compression and destruction process of the rock ($10^5 \sim 10^7$). The above analysis shows that phyllite is a typical brittle rock without obvious plastic yielding behavior. The evolution of the entire damage process of phyllite can be expounded from the perspective of bedding. First, under low stress conditions, the original microcracks and microholes near the surface of the bedding are constantly compacted, and few or no new fractures are produced, resulting in a very weak acoustic emission signal. With the continuous increase in stress, the rock began to produce elastic deformation and accumulate elastic energy. When the stress reaches the peak compressive strength of the specimens, the cracks at the bedding layer begin to sprout, develop and extend rapidly, the shearing or tensile failure zone along the bedding plane releases a large

amount of elastic stress waves, and the failure zones communicate with each other to form a macroscopic fracture surface. Therefore, the acoustic emission signals of phyllite show a steady to steep increasing trend.

4.2.1 Influence of Bedding Angle on AE of Phyllite

Taking the water-bearing phyllite sample as the object of analysis, the vibration characteristics and relationship between the cumulative energy and bedding angles are shown in Fig. 15. Figure 15a shows that the overall trend of the cumulative energy curves of phyllite for the four bedding angles is similar and is roughly divided into three stages: (1) the fast growth stage (S1), in which the time range is mainly between 0 and 300 s. The cumulative energy curve at this stage increases very rapidly with a growth rate of 11.865 J/s at 0°, 18.695 J/s at 30°, 14.905 J/s at 60°, and 142.813 J/s at 90°. (2) In the slow growth phase (S2), the strain energy is continuously stored in the elastic matrix of the phyllite as the stress increases to the elastic deformation stage in the compression curve; hence, the damage of the sample is small, and the cumulative energy curve grows very slowly. (3) In the rapid growth phase (S3), in which the elastic strain stored in the specimen is released rapidly, the microcracks expand and permeate swiftly, and finally, macroscopic cracks are formed. At this time, the AE energy fluctuates considerably, and the rock damage is serious. From Fig. 15a, it can be seen that the rapid growth stages of the specimens for 0° and 90° are very prominent, whereas for the 30° and 60° cases, the curve is more in the form of a "ladder" or "step." The corresponding relationship between cumulative AE energy and stratification is shown in Fig. 15b. With the increase in bedding angle, the cumulative energy shows a "U-shaped" change trend that first decreases and then increases, which is consistent with the variation law of the peak intensity and elastic modulus of Sect. 3.1. This feature reflects the intuitive relationship between the macrofracture and the microfracture mechanism and further shows that the macrofracture is closely related to the internal microstructure and microcracks in the rock.

4.2.2 Influence of Water Content on Acoustic Emission of Phyllite

Taking the phyllite specimen with a bedding angle of 30° as the object of analysis, the variation characteristics and relationship between the cumulative energy and moisture states are shown in Fig. 16.

It can be seen in Fig. 16a that the variation laws of phyllite for the three kinds of water content are similar, namely, they first grow rapidly, then remain unchanged, and finally grow to the maximum cumulative energy in the form of a "step." In addition, it can also be observed that the test piece undergoes the compaction phase–elastic deformation phase–destruction

failure phase from the beginning to the end of loading and corresponds to the AE, which is the "quiet period"–"stability period"–"active period," and the law of energy variation tends to be consistent, only in terms of energy amplitude. Under dry conditions (0%), it is $1.02E + 6$; under watery conditions (1.5%), it is $4.46E + 5$; and under saturated conditions (2.7%), it is $1.76E + 5$. It can be concluded that the final cumulative energy of the phyllite specimens gradually decreases with increasing water content, and the corresponding relationship between the maximum cumulative energy and water content is shown in Fig. 16b.

According to Fig. 16b, the water content has a significant influence on the trend of the cumulative energy of the AE of the phyllite. The main reason for this phenomenon is the high proportion of clay in the mineral composition of phyllite, which is prone to the hydrolysis effect under the action of water. When mineral particles are dissolved by water, the rock matrix space becomes increasingly loose (Fig. 12), and the contact force between particles gradually weakens, resulting in a reduction in the strength and cohesion of phyllite. Therefore, the energy consumption of phyllite specimens under water-bearing and saturated conditions is less than that of phyllite samples under dry conditions, which leads to the change in AE cumulative energy with increasing moisture content.

5 Conclusion

The mechanical properties and fractures of phyllite for different bedding angles and water content were studied by uniaxial compression tests. The stress–strain curves, microcrack propagation, connection process and fracture mode of phyllite under uniaxial compression are simulated with the discrete element code PFC. The microcosmic failure mechanism and micro-progressive damage evolution process of phyllite under the combined action of bedding angle and water content were analyzed by SEM and AE, and the intuitive relationship between the microfracture mechanism and macrofracture of phyllite was analyzed. The following conclusions are drawn:

1. The influence of the bedding angle and water content on the mechanical parameters of phyllite is very significant. From the perspective of the laminae angle, the modulus elasticity of the rocks shows a "U-shaped" variation with increasing laminae angle for the same water content and reaches a maximum at 0° and a minimum at 60°. However, the relationship between the compressive strength of phyllite and the bedding angle does not completely obey the "U-shaped" trend in the strict sense. When the water content of rock is 0%, the variation curve of compressive strength with bedding angle is "U-shaped,"

but when the water content increases 1.5% and 2.7%, the fitting curve between compressive strength and bedding angle shows a nonlinear decreasing trend. From the perspective of water content, the UCS and elastic modulus of the phyllite decrease linearly and monotonously with water content, showing an obvious water weakening effect.

2. Both the bedding angle and moisture content have a significant effect on the failure mode of phyllite. The bedding angle controls the fracture type of phyllite, i.e., the failure type of phyllite at low bedding angles (0° – 60°) is shear failure along the bedding plane, whereas the failure mode at 90° is tension splitting failure, with a small amount of tensile shear failure. The water content mainly affects the number of crack propagations in phyllite.
3. The stress–strain curve and the final failure form obtained by PFC simulation are basically consistent with the test results, indicating the effectiveness of PFC simulation. In addition, the simulation results show that the failure of phyllite is mainly tensile failure, accompanied by a small amount of shear failure. Internal microcracks originate and expand along the diagonal area of the specimen and continue to connect with the increase in external load until macroscopic fracture occurs.
4. The influence of water and bedding on the microstructure and microfracture mechanism of phyllite is significant, which is mainly manifested as follows: under dry conditions, phyllite has a compact layered or flaky accumulation structure, with less developed pores and fissures. Under water-bearing conditions, water flows into the microcracks and micropores of phyllite, promoting the hydrolysis reaction of cement between particles, thereby reducing the degree of cementation between the particles and increasing the degree of relaxation of the matrix space. In addition, water erosion leads to the dissolution of phyllite mineral particles, which intensifies the stress concentration effect at the crack tip, thus inducing the generation and expansion of more original cracks and secondary cracks. The change in bedding angle promotes the formation of internal friction angle differences. In conclusion, the water and bedding angles will change the microstructure and micromechanical parameters of phyllite, induce the formation of microcracks, and eventually lead to the anisotropy of macroscopic mechanical properties.
5. The characteristics of the acoustic emission energy of phyllite are significantly affected by the bedding angle and water content, mainly as follows: the cumulative energy of acoustic emission presents a typical U-shaped trend with respect to increasing bedding angle, with a peak at 0 and 90 and a trough at 60; the cumulative energy of acoustic emission presents a linear decreasing trend with increasing water content, showing an obvious

water weakening phenomenon. In conclusion, the change law of the cumulative energy of phyllite is basically consistent with the change in macromechanical properties, which reveals that the microfracture mechanism of phyllite and the gradual development process of microcracks are the most fundamental reasons for macrofailure and macrofracture.

Acknowledgements This research was supported by the National Natural Science Foundation of China (NSFC, Grant Numbers 51774057 and 52074048).

Data Availability All data used in this study are openly available from corresponding author upon request.

Declarations

Conflict of interest Long-hao Ma, Jie Chen, Yun-Feng Zhao, Chuang Zhang, Rong Liu and Song Ren declare that they have no conflicts of interest.

References

1. Bai, Q.S.; Young, R.P.: Numerical investigation of the mechanical and damage behaviors of veined gneiss during true-triaxial stress path loading by simulation of in situ conditions. *Rock Mech. Rock Eng.* **53**(1), 133–151 (2020). <https://doi.org/10.1007/s00603-019-01898-2>
2. Ji, L.; Lin, M.; Cao, G.; Jiang, W.: A core-scale reconstructing method for shale. *Sci. Rep.* **9**, 1–12 (2019). <https://doi.org/10.1038/s41598-019-39442-5>
3. Yin, X.M.; Yan, E.C.; Wan, L.N.; Liu, L.C.; Peng, B.; Wang, P.Z.: Anisotropy of quartz mica schist based on quantitative extraction of fabric information. *Bull. Eng. Geol. Environ.* **79**(5), 2439–2456 (2020). <https://doi.org/10.1007/s10064-019-01699-5>
4. Li, K.H.; Yin, Z.Y.; Cheng, Y.M.; Cao, P.; Meng, J.J.: Three-dimensional discrete element simulation of indirect tensile behaviour of a transversely isotropic rock. *Int. J. Numer. Anal. Methods Geomech.* **44**(13), 1812–1832 (2020). <https://doi.org/10.1002/nag.3110>
5. Jia, H.L.; Ding, S.; Zi, F.; Li, G.Y.; Yao, Y.: Development of anisotropy in sandstone subjected to repeated frost action. *Rock Mech. Rock Eng.* **54**(4), 1863–1874 (2021). <https://doi.org/10.1007/s00603-020-02343-5>
6. Chen, Z.Q.; He, C.; Xu, G.W.; Ma, G.Y.; Yang, W.B.: Supporting mechanism and mechanical behavior of a double primary support method for tunnels in broken phyllite under high geo-stress: a case study. *Bull. Eng. Geol. Environ.* **78**(7), 5253–5267 (2019). <https://doi.org/10.1007/s10064-019-01479-1>
7. Wu, R.J.; Li, H.B.; Wang, D.P.: Full-field deformation measurements from Brazilian disc tests on anisotropic phyllite under impact loads. *Int. J. Impact Eng.* **149**, 1–12 (2021). <https://doi.org/10.1016/j.ijimpeng.2020.103790>
8. Chen, Z.Q.; He, C.; Xu, G.W.; Ma, G.Y.; Wu, D.: A case study on the asymmetric deformation characteristics and mechanical behavior of deep-buried tunnel in phyllite. *Rock Mech. Rock Eng.* **52**(11), 4527–4545 (2019). <https://doi.org/10.1007/s00603-019-01836-2>
9. Ukritchon, B.; Keawsawasvong, S.: Undrained stability of unlined square tunnels in clays with linearly increasing anisotropic shear



- strength. *Geotech. Geol. Eng.* **38**(1), 897–915 (2020). <https://doi.org/10.1007/s10706-019-01023-8>
10. Xu, G.W.; He, C.; Wang, J.; Zhang, J.B.: Study on the damage evolution of secondary tunnel lining in layered rock stratum. *Bull. Eng. Geol. Environ.* **79**(7), 3533–3557 (2020). <https://doi.org/10.1007/s10064-020-01775-1>
 11. Cai, J.; Du, G.Y.; Ye, H.W.; Lei, T.; Xia, H.; Pan, H.S.: A slate tunnel stability analysis considering the influence of anisotropic bedding properties. *Adv. Mater. Sci. Eng.* **2019**(23), 1–17 (2019). <https://doi.org/10.1155/2019/4653401>
 12. Chang, S.H.; Chen, C.S.; Wang, T.T.: Sediment Sluice Tunnel of Zengwen Reservoir and construction of section with huge underground excavation adjacent to neighboring slope. *Eng. Geol.* **260**, 1–19 (2019). <https://doi.org/10.1016/j.enggeo.2019.105227>
 13. Moussaie, N.; Sharifzadeh, M.; Safiriar, K.; Khosravi, M.H.: A new classification of failure mechanisms at tunnels in stratified rock masses through physical and numerical modeling. *Tunn. Undergr. Space Technol.* **91**, 1–12 (2019). <https://doi.org/10.1016/j.tust.2019.103017>
 14. Wang, Y.P.; Xiong, L.X.: Numerical analysis of the influence of bolt set on the shear resistance of jointed rock masses. *Civ. Eng. J. Tehran* **6**(6), 1039–1055 (2020). <https://doi.org/10.28991/cej-2020-03091527>
 15. Balamuralikrishnan, R.; Saravanan, J.: Effect of addition of alccofine on the compressive strength of cement mortar cubes. *Emerg. Sci. J.* **5**, 155–170 (2021). <https://doi.org/10.28991/esj-2021-01265>
 16. Akulshin, A.; Bredikhina, N.; Akulshin, A.; Aksenteva, I.; Ermakova, N.: Development of filters with minimal hydraulic resistance for underground water intakes. *Civ. Eng. J. Tehran* **6**, 919–927 (2020). <https://doi.org/10.28991/cej-2020-03091517>
 17. Guo, X.L.; Tan, Z.S.; Wang, X.; Li, A.; Ma, Z.J.; Wu, Y.S.: Effect of bedding angle and mineral composition on mechanical properties and fracture behavior of phyllite under unloading confining pressures. *Geotech. Geol. Eng.* **38**(4), 3611–3621 (2020). <https://doi.org/10.1007/s10706-020-01238-0>
 18. Shi, X.S.; Jing, H.W.; Yin, Q.; Zhao, Z.L.; Han, G.S.; Gao, Y.: Investigation on physical and mechanical properties of bedded sandstone after high-temperature exposure. *Bull. Eng. Geol. Environ.* **79**(5), 2591–2606 (2020). <https://doi.org/10.1007/s10064-020-01729-7>
 19. Wen, S.; Zhang, C.S.; Chang, Y.L.; Hu, P.: Dynamic compression characteristics of layered rock mass of significant strength changes in adjacent layers. *J. Rock Mech. Geotech. Eng.* **12**(2), 353–365 (2020). <https://doi.org/10.1016/j.jrmge.2019.09.003>
 20. Wu, Z.H.; Lou, Y.L.; Yin, S.; Wang, A.L.; Liu, H.; Sun, W.J.; Zuo, Y.J.; Chen, B.: Acoustic and fractal analyses of the mechanical properties and fracture modes of bedding-containing shale under different seepage pressures. *Energy Sci. Eng.* **8**(10), 3638–3656 (2020). <https://doi.org/10.1002/ese3.772>
 21. Yin, P.F.; Yang, S.Q.: Experimental investigation of the strength and failure behavior of layered sandstone under uniaxial compression and Brazilian testing. *Acta Geophys.* **66**(4), 585–605 (2018). <https://doi.org/10.1007/s11600-018-0152-z>
 22. Hooker, J.N.; Ruhl, M.; Dickson, A.J.; Hansen, L.N.; Idiz, E.; Hesselbo, S.P.; Cartwright, J.: Shale anisotropy and natural hydraulic fracture propagation: an example from the jurassic (Toarcian) Posidonienschiefer, Germany. *J. Geophys. Res. Solid Earth* **125**(3), 1–14 (2020). <https://doi.org/10.1029/2019JB018442>
 23. Wang, H.; Ren, F.Q.; Chang, Y.: Effect of bedding angle on tunnel slate failure behavior under indirect tension. *Geomat. Nat. Hazards Risk* **11**(1), 428–445 (2020). <https://doi.org/10.1080/19475705.2020.1729870>
 24. Zuo, J.P.; Lu, J.F.; Ghandriz, R.; Wang, J.T.; Li, Y.H.; Zhang, X.Y.; Li, J.; Li, H.T.: Mesoscale fracture behavior of Longmaxi outcrop shale with different bedding angles: experimental and numerical investigations. *J. Rock Mech. Geotech. Eng.* **12**(2), 297–309 (2020). <https://doi.org/10.1016/j.jrmge.2019.11.001>
 25. Ding, C.D.; Zhang, Y.; Hu, D.W.; Zhou, H.; Shao, J.F.: Foliation effects on mechanical and failure characteristics of slate in 3D space under brazilian test conditions. *Rock Mech. Rock Eng.* **53**(9), 3919–3936 (2020). <https://doi.org/10.1007/s00603-020-02146-8>
 26. Liu, S.X.; Wang, Z.X.; Zhang, L.X.: Experimental study on the cracking process of layered shale using X-ray microCT. *Energy Explor. Exploit.* **36**(2), 297–313 (2018). <https://doi.org/10.1177/0144598717736855>
 27. Gu, H.L.; Tao, M.; Li, X.B.; Momeni, A.; Cao, W.Z.: The effects of water content and external incident energy on coal dynamic behaviour. *Int. J. Rock Mech. Min. Sci.* **123**, 1–16 (2019). <https://doi.org/10.1016/j.ijrmms.2019.104088>
 28. Huang, S.B.; He, Y.B.; Liu, G.F.; Lu, Z.X.; Xin, Z.K.: Effect of water content on the mechanical properties and deformation characteristics of the clay-bearing red sandstone. *Bull. Eng. Geol. Environ.* **80**(2), 1767–1790 (2021). <https://doi.org/10.1007/s10064-020-01994-6>
 29. Li, C.M.; Liu, N.; Liu, W.R.: Experimental investigation of mechanical behavior of sandstone with different moisture contents using the acoustic emission technique. *Adv. Civ. Eng.* **2020**(3), 1–10 (2020). <https://doi.org/10.1155/2020/8877921>
 30. Rabat, A.; Tomas, R.; Cano, M.: Evaluation of mechanical weakening of calcarenite building stones due to environmental relative humidity using the vapour equilibrium technique. *Eng. Geol.* **278**, 1–19 (2020). <https://doi.org/10.1016/j.enggeo.2020.105849>
 31. Song, Y.Q.; Ma, H.F.; Li, X.S.; Zheng, J.J.; Yang, M.J.; Fu, H.: Experimental investigation on the influence of water content on mechanical properties and failure characteristics of tuff. *Geotech. Geol. Eng.* **39**(4), 2871–2882 (2021). <https://doi.org/10.1007/s10706-020-01661-3>
 32. Tang, S.B.: The effects of water on the strength of black sandstone in a brittle regime. *Eng. Geol.* **239**, 167–178 (2018). <https://doi.org/10.1016/j.enggeo.2018.03.025>
 33. Yao, Q.L.; Wang, W.N.; Zhu, L.; Xia, Z.; Tang, C.J.; Wang, X.H.: Effects of moisture conditions on mechanical properties and AE and IR characteristics in coal-rock combinations. *Arab. J. Geosci.* **13**(14), 1–15 (2020). <https://doi.org/10.1007/s12517-020-05610-5>
 34. Yu, C.Y.; Tang, S.B.; Tang, C.A.; Duan, D.; Zhang, Y.J.; Liang, Z.Z.; Ma, K.; Ma, T.H.: The effect of water on the creep behavior of red sandstone. *Eng. Geol.* **253**, 64–74 (2019). <https://doi.org/10.1016/j.enggeo.2019.03.016>
 35. Yu, L.Q.; Yao, Q.L.; Li, X.H.; Wang, W.N.; Han, H.; Zhang, M.T.: Experimental study of failure characteristics and fissure propagation in hydrous siltstone. *Arab. J. Geosci.* **13**(13), 1–19 (2020). <https://doi.org/10.1007/s12517-020-05522-4>
 36. Zhao, Y.C.; Yang, T.H.; Xu, T.; Zhang, P.H.; Shi, W.H.: Mechanical and energy release characteristics of different water-bearing sandstones under uniaxial compression. *Int. J. Damage Mech.* **27**(5), 640–656 (2018). <https://doi.org/10.1177/1056789517697472>
 37. Franklin, J.A.: Suggested methods for determining water-content, porosity, density, absorption and related properties and swelling and slake-durability index properties. *Int. J. Rock Mech. Min. Sci.* **16**, 143–151 (1979)
 38. Jiang, D.Y.; Xie, K.N.; Chen, J.; Zhang, S.L.; Tiedeu, W.N.; Xiao, Y.; Jiang, X.: Experimental analysis of sandstone under uniaxial cyclic loading through acoustic emission statistics. *Pure Appl. Geophys.* **176**, 265–277 (2019). <https://doi.org/10.1007/s00024-018-1960-4>
 39. Zhao, Y.F.; Ren, S.; Wang, L.; Zhang, P.; Liu, R.; Chen, F.; Jiang, X.: Acoustic emission and physicomaterial properties of concrete under sulfate attack. *J. Mater. Civ. Eng.* **33**(4), 04021016 (2021). [https://doi.org/10.1061/\(ASCE\)MT.1943-5533.0003572](https://doi.org/10.1061/(ASCE)MT.1943-5533.0003572)
 40. Song, H.H.; Jiang, Y.D.; Elsworth, D.; Zhao, Y.X.; Wang, J.H.; Liu, B.: Scale effects and strength anisotropy in coal. *Int. J. Coal Geol.* **195**, 37–46 (2018). <https://doi.org/10.1016/j.coal.2018.05.006>

41. Song, H.H.; Zhao, Y.X.; Elsworth, D.; Jiang, Y.D.; Wang, J.H.: Anisotropy of acoustic emission in coal under the uniaxial loading condition. *Chaos Solitons Fractals* **130**, 1–7 (2020). <https://doi.org/10.1016/j.chaos.2019.109465>
42. Ma, L.H.; Jiang, X.; Chen, J.; Zhao, Y.F.; Liu, R.; Ren, S.: Analysis of damages in layered surrounding rocks induced by blasting during tunnel construction. *Int. J. Struct. Stab. Dyn.* **21**(7), 2150089 (2021). <https://doi.org/10.1142/S0219455421500899>
43. Ma, L.H.; Lin, F.; Liu, R.; Liu, P.; Xia, G.; Chen, L.C.: Disturbance and control of national strategic gas storage induced by adjacent tunnel blasting. *Front. Earth Sci.* (2022). <https://doi.org/10.3389/feart.2021.807073>
44. ITASCA. Particle flow code, version 5.00.35. Minneapolis, MN, USA: Itasca: 2018.
45. Shen, H.M.; Zhang, Q.; Li, Q.; Li, X.C.; Shi, L.; Shen, N.: Experimental and numerical investigations of the dynamic permeability evolution of a fracture in granite during shearing under different normal stress conditions. *Rock Mech. Rock Eng.* **53**(10), 4429–4447 (2020). <https://doi.org/10.1007/s00603-020-02074-7>
46. Shen, J.Y.; Zhan, S.X.; Karakus, M.; Zuo, J.P.: Effects of flaw width on cracking behavior of single-flawed rock specimens. *Bull. Eng. Geol. Environ.* **80**(2), 1701–1711 (2021). <https://doi.org/10.1007/s10064-020-02029-w>
47. Zhang, Y.P.; Shi, C.; Zhang, Y.L.; Yang, J.X.; Chen, X.: Numerical analysis of the brittle-ductile transition of deeply buried marble using a discrete approach. *Comput. Part. Mech.* **8**, 893–904 (2021). <https://doi.org/10.1007/s40571-020-00375-w>
48. Ersoy, H.; Karahan, M.; Kolayli, H.; Sunnetci, M.O.: Influence of mineralogical and micro-structural changes on the physical and strength properties of post-thermal-treatment clayey rocks. *Rock Mech. Rock Eng.* **54**(2), 679–694 (2021). <https://doi.org/10.1007/s00603-020-02282-1>
49. Liu, J.T.; Yang, Y.; Gu, C.P.; Li, H.D.: Influence of dry heating regime on the mechanical and shrinkage properties of reactive powder concrete. *J. Zhejiang Univ. Sci A* **19**(12), 926–938 (2018). <https://doi.org/10.1631/jzus.A1800394>
50. Mu, Q.Y.; Ng, C.W.W.; Zhou, C.; Zhou, G.G.D.: Effects of clay content on the volumetric behavior of loess under heating-cooling cycles. *J. Zhejiang Univ. Sci A* **20**(12), 979–990 (2019). <https://doi.org/10.1631/jzus.A1900274>
51. Tripathi, A.; Gupta, N.; Singh, A.K.; Mohanty, S.P.; Rai, N.; Pain, A.: Effects of elevated temperatures on the microstructural, physico-mechanical and elastic properties of Barakar sandstone: a study from one of the world's largest underground coalmine fire region, Jharia, India. *Rock Mech. Rock Eng.* **54**(3), 1293–1314 (2021). <https://doi.org/10.1007/s00603-020-02315-9>
52. Yan, D.M.; Ruan, S.Q.; Chen, S.K.; Liu, Y.; Tian, Y.; Wang, H.L.; Ye, T.N.: Effects and mechanisms of surfactants on physical properties and microstructures of metakaolin-based geopolymer. *J. Zhejiang Univ. Sci A* **22**(2), 130–146 (2021). <https://doi.org/10.1631/jzus.A2000059>
53. Wang, H.; Yang, T.H.; Zuo, Y.J.: Experimental study on acoustic emission of weakly cemented sandstone considering bedding angle. *Shock Vib.* **2018**, 1–12 (2018). <https://doi.org/10.1155/2018/6086583>
54. Zhang, S.W.; Shou, K.J.; Xian, X.F.; Zhou, J.P.; Liu, G.J.: Fractal characteristics and acoustic emission of anisotropic shale in Brazilian tests. *Tunn. Undergr. Space Technol.* **71**, 298–308 (2018). <https://doi.org/10.1016/j.tust.2017.08.031>
55. Hu, X.J.; Xie, N.; Zhu, Q.Z.; Chen, L.; Li, P.C.: Modeling damage evolution in heterogeneous granite using digital image-based grain-based model. *Rock Mech. Rock Eng.* **53**(11), 4925–4945 (2020). <https://doi.org/10.1007/s00603-020-02191-3>
56. Liu, Y.; Ma, T.S.; Wu, H.; Chen, P.: Investigation on mechanical behaviors of shale cap rock for geological energy storage by linking macroscopic to mesoscopic failures. *J. Energy Storage* **29**, 1–15 (2020). <https://doi.org/10.1016/j.est.2020.101326>
57. Jiang, X.; Jiang, D.Y.; Xian, X.F.; Salje, E.K.H.: Collapsing minerals: Crackling noise of sandstone and coal, and the predictability of mining accidents. *Am. Miner.* **101**, 2751–2758 (2016). <https://doi.org/10.2138/am-2016-5809CCBY>

